

A thermal finite element model with efficient computation of surface heat fluxes for directed-energy deposition process and application to laser metal deposition of IN718

Kerem Dortkasli^{a,b}, Murat Isik^{a,b,c}, Eralp Demir^{d,*}

^a*Faculty of Engineering and Natural Sciences, Sabanci University, Tuzla, 34956 Istanbul, Turkey*

^b*Integrated Manufacturing Technologies Research and Application Center, Sabanci University, Tuzla, 34956 Istanbul, Turkey*

^c*Department of Automotive Engineering, Gorukle, 16059 Bursa, Turkey*

^d*Department of Mechanical Engineering, University of Bristol, Bristol, BS8 1TR, UK.*

Abstract

In this study, a numerically efficient thermal finite element process model is developed to predict the melt-pool characteristics of directed-energy deposition (DED) process. The model uses a new technique to compute the effective surface heat loss terms in the form of a volumetric heat sink term in order to avoid the redefinition of surface heat fluxes from the free-surfaces after addition of every layer. In addition, thermal model incorporated the heat losses due to evaporation and Marangoni effect by changing the conductivity at the liquid state. The melt pool dimensions of IN718 were experimentally measured by in-situ thermal monitoring and by ex-situ optical microscopy of the cross-sections of the deposited tracks. The proposed model accurately predicts the experimental melt-pool dimensions of single-track and multi-layer depositions over the range of process parameters.

Keywords: directed-energy deposition, thermal process simulation, FEM, IN-718

1. Introduction

Metal additive manufacturing (AM) has received an increasing attention in the recent decades due to its various advantages over conventional manufacturing processes [1, 2] because it permits manufacturing of complex geometries, reduces number of manufacturing steps, integrates with the digitization, banishes machine tools, lubricants, and molds for environmentally safe manufacturing.

Metal AM methods can be mainly categorized into two processes as the directed energy deposition (DED) [3] and powder bed fusion (PBF) [4] in addition to the lithography methods [5]. In the DED processes, the heat source; laser, electron beam, or electric arc, supplies the energy simultaneously with the feed stock material that is powder or wire [6]. In PBF method however, the heat source (laser or electron beam) selectively melts the powder layer [7]. DED processes are used to manufacture parts/components with large

*Corresponding author

Email address: eralp.demir@bristol.ac.uk (Eralp Demir)

dimensions due to their higher deposition rates (5-30 g/min) in comparison to PBF processes (2-3 g/min). DED process have been extensively used in laser cladding or coating applications [8, 9]. DED has also been used in simultaneous repair processes [10, 11]. DED made it possible to manufacture functionally gradient materials which is practically very difficult and limited in terms of the alloy composition for the PBF process. Although the high manufacturing rates of DED makes it a better choice over PBF, the geometrical tolerances of as-build parts are relatively poor in comparison to the PBF processes. For this reason, DED process was usually combined with other conventional subtractive manufacturing methods to achieve the desired geometrical requirements which makes it a hybrid process indeed [12]. The majority of the studies have focused on process parameter optimization for improving the mechanical response of various type of materials that were produced by DED processes[13] including Titanium alloys [14]. Therefore, the advantages of DED is hindered by the inevitable defects and porosity that deteriorate the mechanical properties demanding a rigorous process parameter optimization study [15].

Numerical simulations of the AM process help to minimize the tedious experimental trial and error methods to optimize the process parameters for the best functional properties. Thermal simulations relay melt-pool dimensions (i.e. penetration depth, the overlap of melt zones, phases, etc.) given the material parameters and process parameters. Accordingly thermomechanical process simulations reveal the distortions and residual stresses [16]. Simulations have been used to understand the effect of process parameters on temperature and residual stress profiles after the deposition [17]. Thermomechanical process models tell a better understanding of the effect of different process parameters such as scan lengths [18], scan patterns [19, 20], and laser spot size [21]. Further new approaches benefit from the cyclic plasticity curves for accurate estimation of residual stresses [22]. The numerical model findings were occasionally validated by experimental measurements [23, 24]. The effect of residual stresses while still is a major concern, residual stresses have relatively lower magnitudes for DED processes than PBF processes. Because in the DED process the baseplate can be preheated up to high temperatures reducing the temperature gradients between the baseplate and the build material, thereby decreasing the residual stresses.

Finite element process models for AM processes are very similar to that of the weld models [25]. For example, the majority of the thermal process simulations use a double ellipsoid heat source model of [26] similar to the welding process models. Weld models use a moving heat source in conjunction with layerwise activation of element methods as the modeling technique for multi-pass welding process similar to AM [27]. Element activation methods are classified into three different categories as quiet-element, active/inactive-element, and hybrid methods [28]. Quiet elements are always present in the finite element mesh and included to the analysis at every time increment but with ineffective physical properties [28] which were used to simulate DED process for Ti6Al4V [29, 30]. However, the deactivated build elements are not included in

the finite element analysis until they were activated in the active-inactive element method. The activation criteria that depends on the position of heat source for any location in the model using a threshold for the energy density [16]. Recently, more sophisticated hybrid methods were developed for computational efficiency [31].

Multi-physics process simulations of the DED process revealed accurate prediction of melt-pool dimensions and shape with the cost of simulation times. These simulations considered the initial powder state, liquid phase of the melt-pool and the corresponding fluid dynamics as well as solidified state. Multi-physics simulations suggested newer predictions such as phases and their distribution [32] other than melt-pool geometry. For example, [33] used process simulations to estimate dynamic pore formation. In addition, [34] multi-physics simulations for melt-pool dynamics and used process simulations to predict the morphological texture of the microstructure of the deposit as equiaxed or columnar. Similarly, microstructures for different process parameters were predicted using temperatures of the process simulations [35] also in conjunction with solidification models [36]. A detailed summary of different approaches for more accurate modeling of the DED process can be found in the reference [37].

In-situ temperature monitoring has been used to examine thermal cycling phenomena during manufacturing for validation of the thermal models [38, 39]. Indeed many of the commercial DED platforms use different optical in-situ thermal measurements to monitor melt-pool temperatures [40]. Thermocouples were used in research studies for experimental validation of the temperatures during metal deposition [41]. Temperature evaluation during the melting was validated also by different non-contact measurement systems such as; infrared (IR) temperature sensors [42] and pyrometers [43]. Consequently, customized DED systems equipped with an IR temperature monitoring system were used to identify optimum nozzle-sample working distance [44]. In addition, in-situ surface strains were measured of a DED process using Digital Image Correlation (DIC) method [45]. Experimental validation studies include analysis of cross-sections of 3D-printed samples to measure melt-pool dimensions; melt-pool depth, dilution, and melt-pool width. [46] defined dilution as the fraction of the material that penetrates the substrate relative to the overall depth of the build.

In this study, a novel thermal finite element model is developed using a commercial finite element software and its user-defined subroutines. The proposed approach uses element activation methods including temperature and state-dependent material properties to perform accurate simulations of the DED process. The novel features of the model are:

- Treatment of surface losses as a volumetric heat sink to eliminate the need for the re-definition of traction-free surfaces after the addition of each layer,
- Evaporative surface heat losses,

- Marangoni effect by changing the thermal conductivity of liquid state along with the feed and build directions.

The experimental investigation of the temperatures and melt-pool sizes using the in-situ thermal imaging system as well as ex-situ analysis of the cross-sections that were obtained from the cross-sections of the melt zones for different process parameters are used to provide a comparison to the process simulations. Moreover, melt-pool dimensions of multi-layer depositions with different process parameters are investigated together with the simulation findings to predict the inter-layer fusion boundaries.

2. Experiments

DED experiments were performed with DMG-MORI[®] Lasertec 65 3D hybrid system equipped with both AM and five-axis milling capabilities. The machine had a Coax 14 powder nozzle and a 1020 nm continuous-wave diode laser with a maximum power of 2500 W, Fig. 1. The powder particles that were transported through a nozzle with argon gas. Subsequently, melted particles were deposited on a stainless-steel (SS316-L) substrate/baseplate.

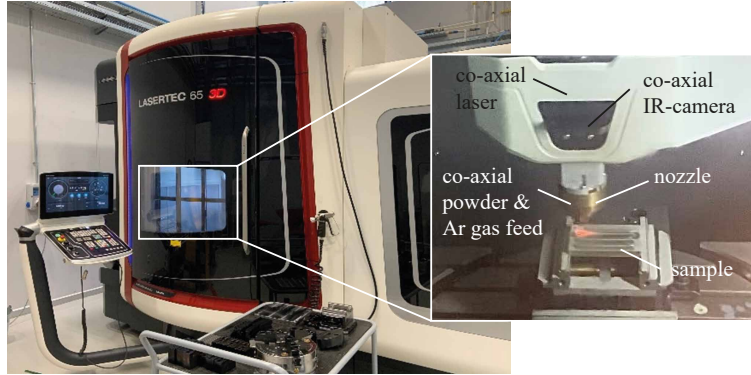


Figure 1: DMG MORI Lasertec 65 3D hybrid additive and subtractive manufacturing machine that was used to manufacture the test samples in this study.

Inconel 718 (IN718) metal powder was used as the build (or deposited) material. Gas atomized powder material was mostly spherical and ranged in size from 45 to 90 μm . The chemical composition of IN718 powder contains 52.5% Ni, 19% Cr, 18% Fe, 5% Nb, 3% Mo, 1% Ti, and 0.5% Al.

IN718 was built or deposited over the SS316-L baseplate with the dimensions of 100 mm \times 60 mm \times 10 mm in length \times width \times thickness, respectively. The parallelism of the baseplate was maintained by milling of top and bottom surfaces using the milling system of the same manufacturing platform. Finally, the baseplate surface was cleaned by first blowing compressed air and then using ethanol prior to the DED fabrication.

The deposition in the form of single tracks with the dimensions of 80 mm \times 3 mm \times 0.45 mm for length \times width \times thickness, respectively. Three single tracks were manufactured for each parameter using a total of nine different processing parameters. Table 2 shows laser power and scan speed as the process parameters that were used in experiments and simulations.

Parameters excluding the laser power and scan speed remained constant throughout the experiments. The stand-off (working) distance was set to the default value of 13 mm, while the laser spot diameter (top head diameter) was set to 3 mm in focus, and the powder flow rate was maintained as 15 g/min for all single track experiments. The flow rates of protective shielding and carrier argon gas were set to 5 L/min and 6 L/min, respectively. The baseplate temperature was kept constant at 323 K during all of the experiments by the heating system available within the DED platform.

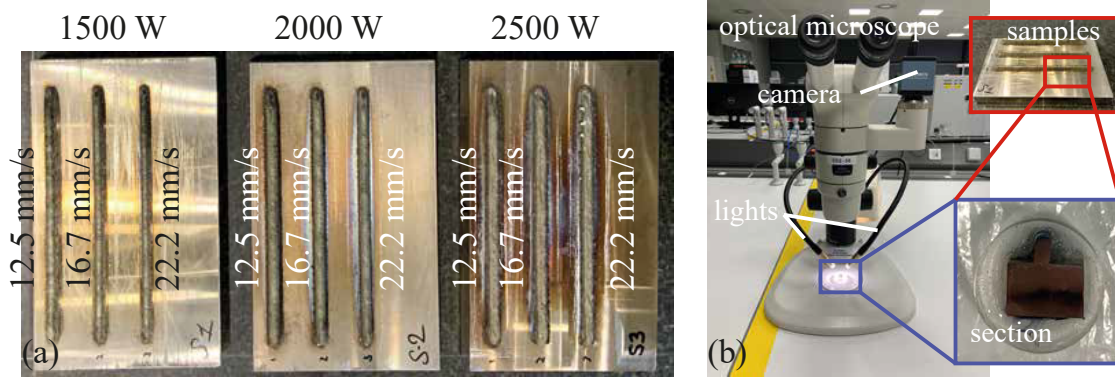


Figure 2: (a) Test samples that were produced at different process parameters; scan speed and laser power, (b) Sample preparation steps sectioning, polishing, and etching of the samples, and Nikon LV100ND optical microscope system that was used in the analysis.

Fig. 2(a) shows single-track deposits for a variety of process parameters; scan speeds of 12.5 mm/s, 16.7 mm/s and 22 mm/s and laser power levels of 1500 W, 2000 W and 2500 W. The effect of scan speed on the track widths was negligible for the samples with the same laser power. On the other hand, increasing laser power promoted an increase in the track width. This effect became even more prominent on the tracks layers at a power rating of 2500 W.

Fig. 2(b) shows the optical microscopy (OM) analyses on the cross-sections of the single track deposits. Samples were sectioned along the longitudinal direction (x-axis) nearly at the center of the build in order to measure the melt-pool dimensions. Samples were cut by using water jet cutting and the deposited parts were left on the substrates in as-build condition and 6 mm thick sections. All cross-sections were mounted into epoxy-resin material those were subsequently wet-ground using SiC grinding papers down to 4000 grit. After that, the samples were polished using 1 μ m aluminum-oxide suspension. A solution containing 40% HCl (hydrochloric acid), 30% CH₃COOH (acetic acid), and 30% HNO₃ (nitric acid) was prepared for chemical

etching. Etching was then performed by the prepared chemical solution for 15 seconds to expose melt-pool geometry and microstructural features. The etched surfaces were then investigated using Nikon LV100ND optical microscope. Geometric dimensions of the height and width of the cross-sectional areas for deposited and substrate materials were determined using Clemex Vision measurement software.

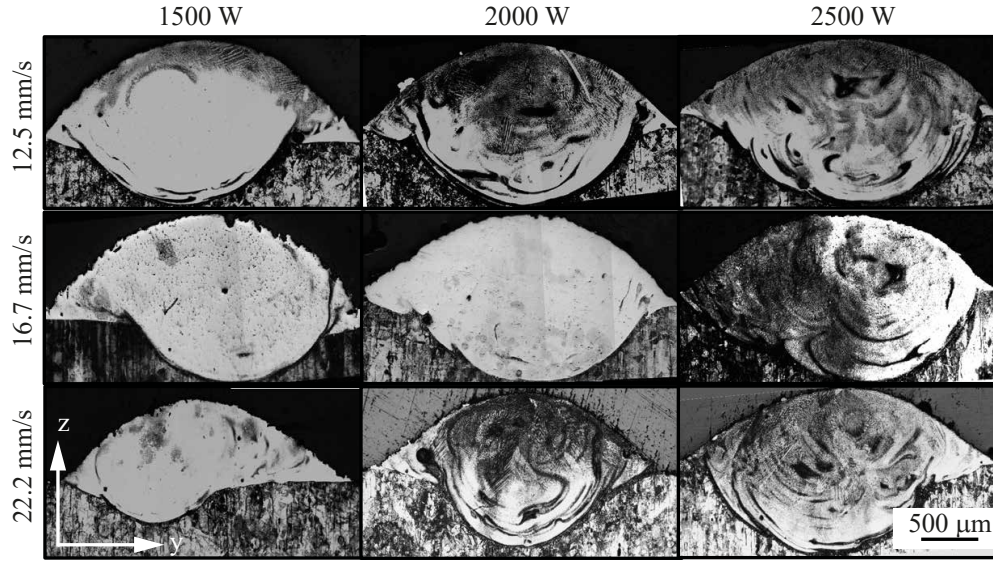


Figure 3: Cross-sections of single-track deposition for different process parameters by optical microscopy.

Fig. 3 shows the images that were obtained from the cross-sections of the single-tracks manufactured using different laser power and scan speed. Qualitative investigation of the images reveals several important observations. The width of the melt-pool increased with increasing laser power whereas the increase in the laser power caused widening of the track profile along the transverse direction (y-direction). The penetration depth was noticeably low for the case with the lowest energy (1500 W) and the highest speed (22.2 mm/s). Ramping up the laser power while keeping the scan speed constant (22.2 mm/s) resulted in an increase in the penetration depth. This effect was not observed for the sample processed with other processing speeds, hence 22.2 mm/s can be assumed as a critical scan speed that needs to be attained to ensure the fusion of deposited layer onto the layer underneath. The penetration was not symmetrically aligned with the axis of the melt-pool. The source of this offset is not precisely known.

Fig. 4 illustrates in-situ thermal camera images that were captured at approximately the center location of the single-track deposits where the deposition process is expected to reach its steady-state behavior. The image collection frequency was giving at least a thousand images during a single layer deposit. However, the thermal images of the melt-pool did not exhibit significant difference except right at the start or at the end of the track. These images were then converted to temperatures using the calibration scale of the system given by the system supplier. The dimensions of the images were the same for all of the plots. As

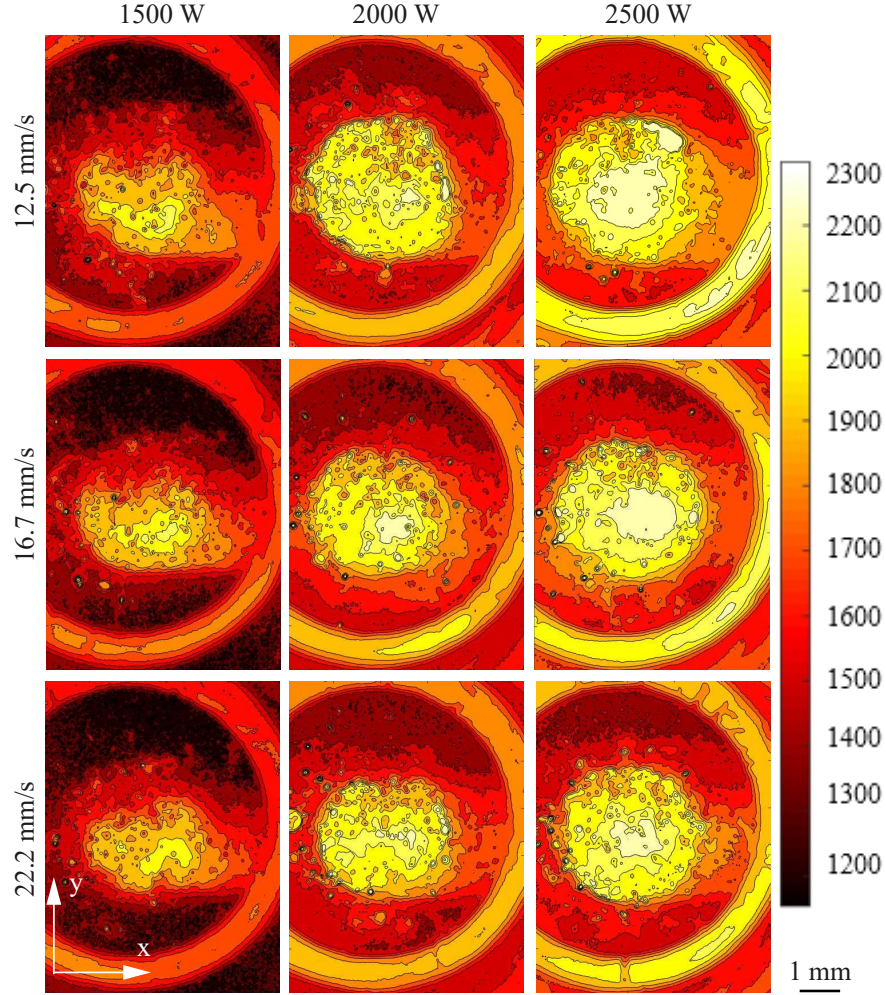


Figure 4: In-situ IR thermal imaging co-axial to the laser beam. Top view of the melt-pool for different process parameters.

the laser power increased, the maximum temperature also increased thereby leading to the enlargement of the size of the melt-pool. Accordingly reducing the scan speed resulted in an increase in the dimensions of the melt-pool, especially in the width direction by expanding the size of the melt zone along the transverse direction (y-axis). The laser power had a much more significant effect on the geometry of the melt zone and also on the temperatures in comparison to the scan speed. The size of the region over temperatures of 2000 K became larger as the laser power increased.

Multiple-layer deposits were investigated to further understand the effect of process parameters on the fusion of subsequent layers. The inter-layer fusion is relatively more important to understand than the fusion to the baseplate material because the baseplate connection will be removed at the final manufacturing stage anyway. For this reason, single track walls with a total of eight number of layers were manufactured, Fig. 5. The deviation from straightness of the wall geometry increased as the laser power increases. Because, increasing laser power up to 2000 W has led to re-melting of nearly all of the formerly deposited layers. This

was referred as the overheating phenomenon that increases the size of the melt zone. Therefore, the layers that fuse deeper into the substrate dramatically decrease the final height of the walls. The use of higher laser power greater than the 2000 W level resulted in significant dimensional deviations in the height and width of wall. Accordingly, the microstructures were coarsened because of the very large size of the melt zone in comparison to the layer thickness that is clearly noticeable from the micrographs at the highest laser power, Fig. 5(g)-(i). The scan speed had an inverse relationship with the wall height as expected since the powder flow rate was kept constant during the experiments. However, the scan speed influenced the shape irregularity of the melt zone that also had an overall effect on the wall height. The scan speed shall be selected to be slow enough to have a regular melt zone yet fast enough not to cause overheating and defect formations. Accordingly, the best dimensions for the wall geometry were obtained at the scan speed of 16.7 mm/s, Fig. 5(b).

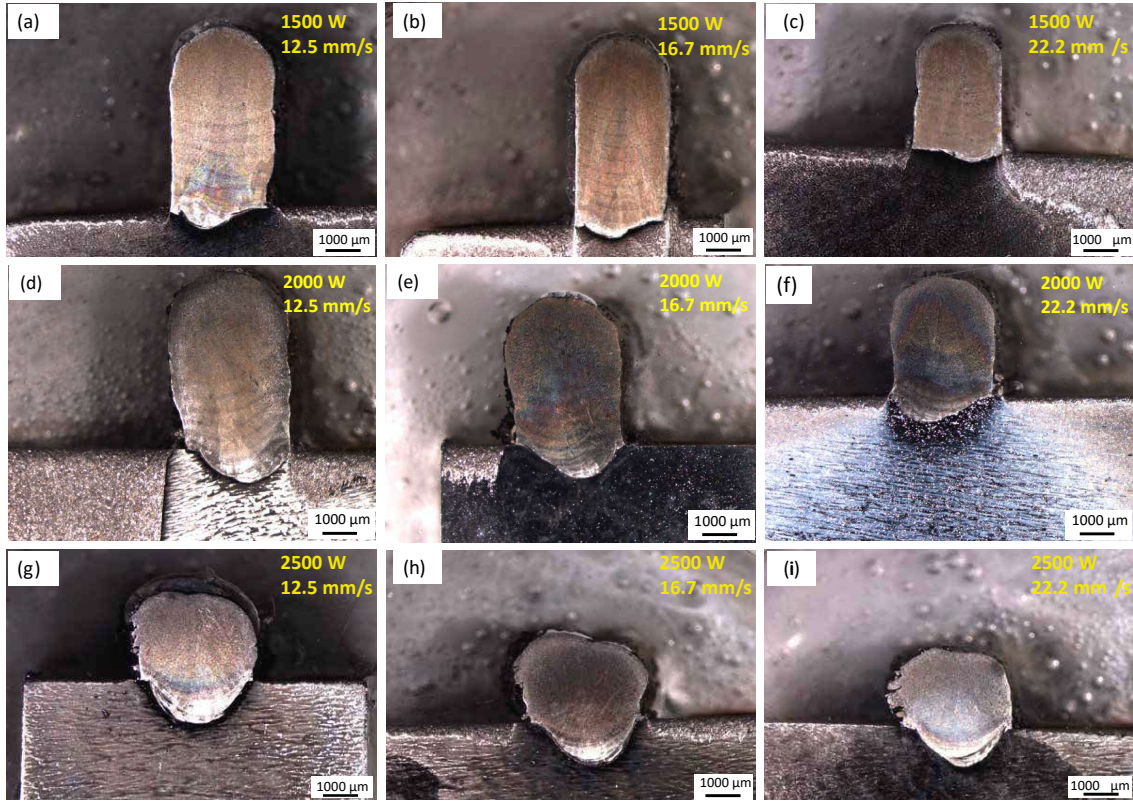


Figure 5: DED melt-pool micrographs for process parameters of (a) 12.5 mm/s - 1500 W, (b) 16.7 mm/s - 1500 W, (c) 22.2 mm/s - 1500 W, (d) 12.5 mm/s - 2000 W, (e) 16.7 mm/s - 2000 W, (f) 22.2 mm/s - 2000 W, (g) 12.5 mm/s - 2500 W, (h) 16.7 mm/s - 2500 W, (i) 22.2 mm/s - 2500 W.

The layer height does not remain constant during the process although the layer thickness was set to a constant value (0.45 mm) since a constant powder flow rate was used. An indicatpr called the comparison parameter was used in the literature [47] to provide a measure for the unit energy supplied to the material. Eq. (1) shows the correlation parameter, S ($\text{W min}^2 \text{g}^{-1} \text{mm}^{-1}$), in which P , \dot{m} , and v represent the laser

power (W), powder flow rate (g/min), and scan speed (mm/min), respectively [47]. The wall height or layer thickness can be compensated by adjusting the powder flow rate while keeping the correlation parameter constant.

$$S = \frac{P}{v \dot{m}} \quad (1)$$

Table 2 includes the comparison parameter values for the process conditions and the overall wall heights of the multiple-layer deposit for a constant powder mass flow rate of 15 g/min. The wall heights were measured from the optical micrographs of the cross-sections, Fig. 5, with respect to the baseplate level.

Table 1: Process parameters used in single and multiple-layer deposits; laser power, scan speed. Wall heights for multi-layer deposits and corresponding comparison parameter, S .

scan speed [mm/s]	laser power [W]	exp. wall height [μm]	S [$\text{W min}^2 \text{g}^{-1} \text{mm}^{-1}$]
12.5	1500	6029	8.00
12.5	2000	5118	10.67
12.5	2500	2853	13.33
16.7	1500	6265	5.99
16.7	2000	4235	7.98
16.7	2500	2765	9.98
22.2	1500	3971	4.50
22.2	2000	3735	6.01
22.2	2500	2441	7.51

The correlation parameter, S , and layer thickness can be well related to one another, Fig. 6. The same data points are shown with two different graphs that indicate constant scan speed and constant laser power contours in different colors. The correlation parameter and process parameters within the optimum range of process parameters were linear.

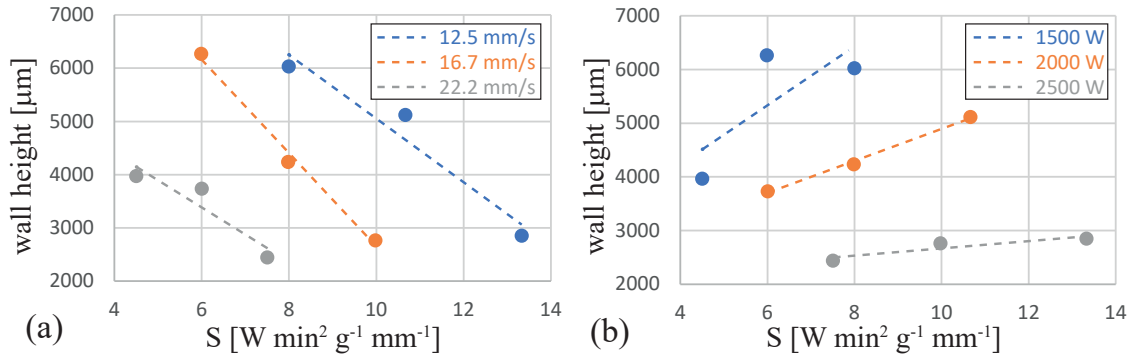


Figure 6: Total wall height vs. correlation parameter for multiple-layer deposits. The line fits indicate constant (a) scan speed and (b) laser power.

The optimum process parameters for multiple-layer deposits were obtained at the lowest laser power

(1500 W) and moderate scan speed (16.7 mm/s). This parameter set resulted in the tallest wall height. The optimum scan speed was within the range of selected values. This can also be concluded from the layer height which increases and then decreases for the same power level values as S decreases from the value of 14 to 4, Fig. 6(a). The lowest laser power resulted in the highest wall height in Fig. 6(b).

Ideally a constant layer thickness value was set in the DED platform before manufacturing while the experimental layer thicknesses were significantly different. The experimental results show a clear variation of layer heights as the process parameters change. The machine did not employ a compensation, such as adjusting the powder flow rate, to correct these dimensional errors. The user has to manually enter these corrections in case needed. For this reason, correlation parameter could be used for tuning process parameters by keeping the unit energy density supplied to the material the same. In this study, the effect of laser power and scan speed as the process parameters were investigated only, although the mass flow rate of powder could have been optimized to obtain constant layer height. However, this required further experimental investigation and parameter optimization studies as in the reference [47]. Therefore, the machine default value for powder mass flow rate was used to avoid porosity and lack of fusion defects.

3. Model

The following sections describe the thermal model, process parameters, time stepping algorithm, finite element model, and element activation method, respectively.

3.1. Thermal Model

The thermal model seeks for the transient temperature field using energy balance, the local form of which is shown in Eq. (2). ρ , C_p , T , \mathbf{q} and \dot{Q} represent mass density, specific heat, temperature, heat flux vector, and heat input, respectively. The heat flux vector and heat input are computed at any position \mathbf{x} and at any time t .

$$\rho C_p \frac{\partial T}{\partial t} = -\nabla \cdot \mathbf{q}(\mathbf{x}, t) + \dot{Q}(\mathbf{x}, t) \quad (2)$$

Goldak's double ellipsoid model is used as the heat input as shown in Eq. (3). \dot{Q} is the heat input per unit volume, P is the laser beam power and η is the lumped efficiency factor. r_x , r_y , and r_z represent the laser spot radii in x , y , and z directions, respectively.

$$\dot{Q}(\mathbf{x}, t) = \frac{6 \eta \sqrt{3} P}{\pi \sqrt{\pi} r_x r_y r_z} \exp\left[-\left(\frac{3x^2}{r_x^2} + \frac{3y^2}{r_y^2} + \frac{3z^2}{r_z^2}\right)\right] \quad (3)$$

The heat flux vector, \mathbf{q} , is computed using the temperature gradients and conductivity, \mathbf{k} via Eq. (4).

$$\mathbf{q}(\mathbf{x}, t) = -\mathbf{k} \nabla T \quad (4)$$

Heat loss by convection occurs from the top surfaces of the deposited layers due to Argon gas supply during the DED process. The corresponding heat transfer rate from the surfaces, \dot{q}_{conv} , is computed using an effective convection coefficient, h_{con} , and ambient temperature, T_{amb} , by Eq. (5). Forced-convection is used on the top surfaces of the newly deposited elements while free-convection on the exposed baseplate surfaces are assumed in the analysis.

$$\dot{q}_{con}(\mathbf{x}_s, t) = h_{con} (T - T_{amb}) \quad (5)$$

Radiative heat loss, \dot{q}_{rad} , from the exposed surfaces is computed using Eq. (6) in which ϵ and K_B are the emissivity and Boltzmann constant. Radiative losses are only considered for the last deposited layer.

$$\dot{q}_{rad}(\mathbf{x}_s, t) = K_B \epsilon (T^4 - T_{amb}^4) \quad (6)$$

Eq. (7) shows the calculation of evaporative heat losses, $\dot{q}_{eva}(\mathbf{x}_s, t)$, in accordance with the reference [48]. ΔH_ν^* , M , R , T_s , T_ν , P_0 are the effective enthalpy of metal vapor, molar mass of metal vapor, universal gas constant, temperature of the surface, boiling temperature, and atmospheric pressure, respectively. Evaporative heat losses are only applied to the last deposited layer.

$$\dot{q}_{eva}(\mathbf{x}_s, t) = \frac{0.82 \Delta H_\nu^*}{\sqrt{2 \pi M R T_s}} P_0 \exp\left(\frac{\Delta H_\nu^* (T_s - T_\nu)}{R T_s T_\nu}\right) \quad (7)$$

The effective surface loss, \dot{q}_{eff} , is computed as the sum of convective, radiative, and evaporative surface losses.

$$\dot{q}_{eff} = \dot{q}_{con} + \dot{q}_{rad} + \dot{q}_{eva} \quad (8)$$

The surface heat losses were expressed as a volumetric heat loss term for simplicity. This is explained in the finite element model section in detail.

3.2. Process Parameters

Table 3.2 shows the same experimental process parameters used in this study for IN718. Process parameters include laser power (P), scan speed (v), return speed (v_r) that is used to calculate the dwell time between layers, laser beam radius (r), layer thickness (d), free convective coefficient (h_{conv}), forced convective coefficient (h_{forc}), and the ambient temperature (T_{amb}).

Table 2: Process parameters that were used in the simulations.

description	parameter	unit	value
laser power	P	W	1500, 2000, 2500
scan speed	v	mm/s	12.5, 16.7, 22.2
return speed	v_r	mm/s	50
beam radius	r	mm	1.5
layer thickness	d	mm	0.45
free convective coefficient	h_{conv}	W/m ² /K	15
forced convective coefficient	h_{forc}	W/m ² /K	35
ambient temperature	T_{amb}	K	298

Efficiency factor, η , had a significant effect on the temperature distributions. A constant value for η of 0.6 was used in this study. This value was obtained by several simulations that reveal the best matching the observed maximum temperature between the experiments and simulations for a single-track case. The highest power (2500 W) and lowest scan speed (12.5 mm/s) was used for this calibration that resulted in the highest temperatures.

3.3. Time stepping

Time increment is an essential parameter for the accuracy and efficiency of the process simulations. Using constant time step makes the simulation computationally relatively inefficient. This is related to the small time steps required for convergence at the start or re-start of heat source during transient regime. But after the heat source entry or exit, convergence to reach steady-state temperatures is attained at larger time steps. In AM, the entry or exit of the heat source may happen many times depending on not just the number of layers but also on the size and geometry of the part to be manufactured. For this reason, an automatic time stepping algorithm is needed for AM process simulations. For this reason, a temperature convergence tolerance value, ΔT , of 50 K is specified with two additional constraints.

Constraint-1: The time increment, Δt , shall be less than a critical value to ensure that it remains within the heat affected element between two time steps. This will avoid the temperature jumps between the elements and provide continuous activation of elements. Inequality (9) is the upper bound for time increment in which r_x and v are the element size along the scan direction and the speed of the heat source, respectively.

$$\Delta t < \frac{r_x}{v} \quad (9)$$

Constraint-2 To ensure Inequality (9), the time step, Δt , is multiplied with a factor, f_{op} , as in Eq. (16), similar to the reference [49]. An upper limit according in Eq. (10) is used in the simulations.

$$\Delta t = f_{op} \frac{r}{v} \quad (10)$$

3.4. Finite Element Model

Finite element method provides solution of global (weak) form of energy balance in Eq. (2) by discretizing temperatures as the field variables. A commercial finite element solver is used with user-subroutines.

Fig. 7 shows the mesh and the boundary conditions used in the simulations for a single-track deposition that consists of 14,520 elements and 18,166 nodes for the scan speed of 12.5 mm/s. The number of elements depends on the scan speed, hence the number of elements and nodes in the mesh are different for various cases. Different material properties are used for the baseplate and deposited layer, Fig. 7(a). The baseplate temperature is kept at 323 K as in the experiments. The baseplate temperature is applied as an initial condition for all of the elements in the mesh Fig. 7(b), and as a boundary condition at the bottom most surface of the baseplate, Fig. 7(c). Moving volumetric heat flux is employed to all of the elements in the mesh, Fig. 7(c).

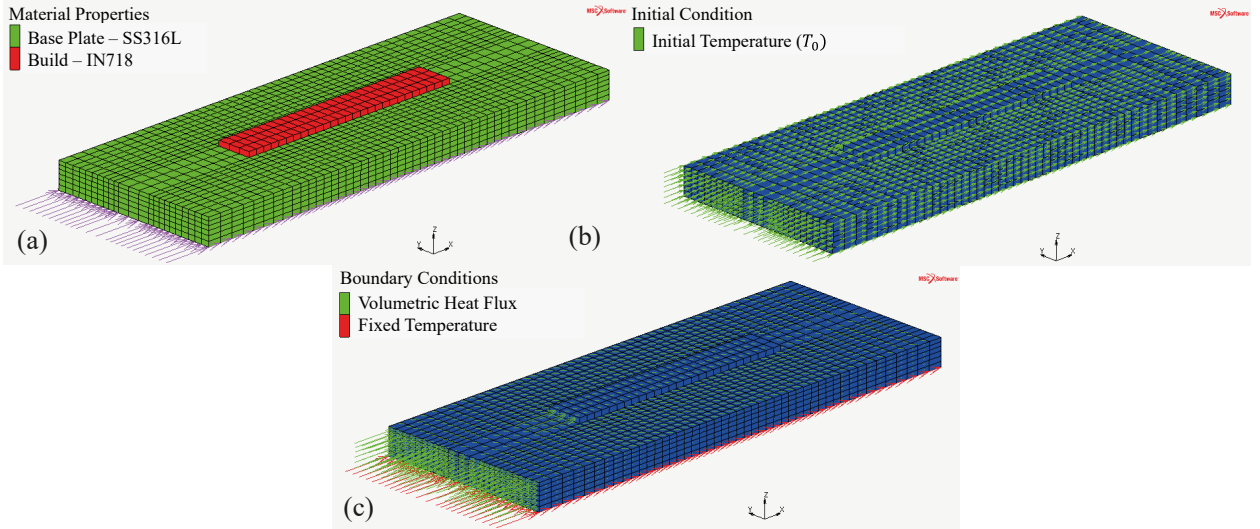


Figure 7: (a) Material types (initial conditions), (b) initial and (c) boundary conditions.

The element size is determined using the limit on the time increment as shown in the Inequality (9). The heat source shall remain within the element during a time step of the motion of the heat source. An additional mesh refinement factor, f_{ref} , is used during model to ensure this criterion ($0 \leq f_{op} \leq 1$) as in Eq. (11).

$$\Delta x = \frac{r_x}{f_{op} f_{ref}} \quad (11)$$

The baseplate material properties are assumed to be temperature-dependent as shown in Table 6 in the Appendix section. The use of temperature-dependent baseplate properties for SS316L instead of constant thermal properties revealed more realistic simulation findings, hence temperature-dependent physical properties are also used for the baseplate in the simulations.

The finite element model is implemented in MSC MARC[®] commercial finite element software. Several user-defined subroutines are used altogether to simulate the DED process which are listed in the below [50].

- FLUX: to define the position and magnitude of the moving heat flux
- UBINC: to update the state variables at the beginning of each increment
- UACTIVE: to determine the active or inactive elements based on a criteria
- ANKOND: to define anisotropic conductivity at liquid or solid states
- USPCHT: to define the specific heat or heat capacitance
- INTCRDS: to find the integration point coordinates once at the initialization
- UTIMESTEP: to set the maximum allowable time increments during deposition and dwell periods

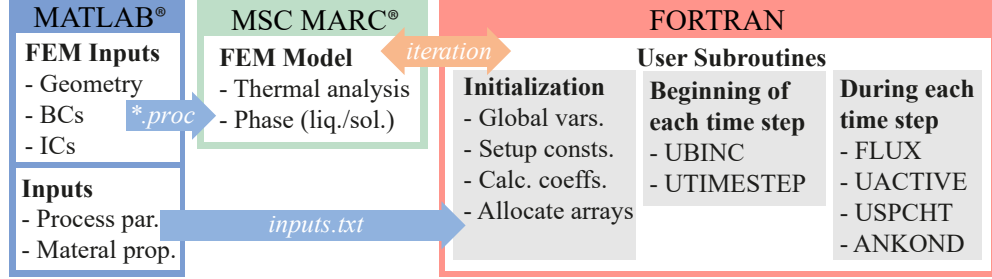


Figure 8: Flowchart of different software environments used for the generation of the inputs (MATLAB[®]), finite element analysis (MSC MARC[®]), together with user defined subroutines (Fortran).

In the current study, a new strategy is followed to define the surface heat losses, Eq. (8). At first, the topmost elements are identified by the position of the moving heat source and the coordinates of the integration points of elements. Surface boundary conditions of these elements are expressed in the form of a negative volumetric heat source term for the topmost elements of the newly added layer. Divergence theorem is used to convert surface integrals to a volumetric integral as shown in Eq.(12) in which \mathbf{q}_s represents the heat losses from the surface.

$$\int_V \nabla \cdot \mathbf{q}_s dV = \oint_S \mathbf{q}_s \cdot \mathbf{n} dS \quad (12)$$

To prove the Eq. (12), consider the heat loss for a topmost (or newly) deposited element shown in Fig. 9. The surface heat flux in Eq. (12) simply becomes as in Eq. (13) at which A and Q_s represent the area of the topmost surface and the amount of heat loss, respectively.

$$\dot{Q}_s = q_{eff} A \quad (13)$$

Recalculating the same heat loss Q_s using the divergence theorem, which is a function of the heat flux gradient along the build direction reveals Eq. (14). V represents the total volume for the element. This expression brings us back to the same expression obtained from the surface fluxes in (13).

$$\dot{Q}_v = \frac{q_{eff} - 0}{d} V = \frac{q_{eff}}{d} A d = q_{eff} A \quad (14)$$

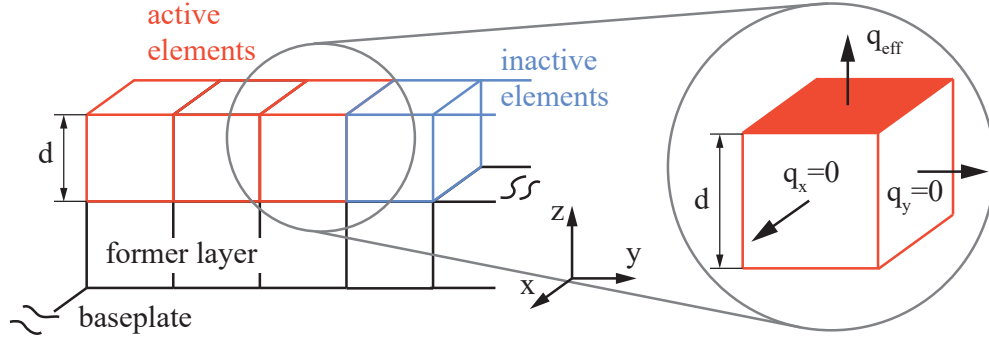


Figure 9: Schematic sketch of the finite element model with baseplate, active and inactive build elements and surface heat losses.

The effective surface heat loss including forced-convection is applied only on the top surfaces of the deposited elements, Fig. 9. Assuming an effective scalar heat flux of q_{eff} for elements with of thickness d , the divergence theorem reveals the surface heat losses in the form of a volumetric heat loss term as in Eq. (15).

$$\dot{Q}_{eff} = -\frac{q_{eff}}{d} \quad (15)$$

This way the surface heat losses are converted to volumetric heat losses. Therefore, the use of a separate subroutine (FILM) to define the surface heat losses and also the need for identification of free surfaces after the addition of each layer are both eliminated which made the analysis much more efficient. This allowed the using FLUX subroutine also to define the surface heat losses.

The effective heat loss with forced convection (h_{forc}) is applied to the topmost deposited elements only. Therefore, the convective losses from the sides are neglected. The natural convection (h_{conv}) is assumed to

be present on the topmost baseplate elements throughout the simulations.

3.5. Element Activation

The build elements are deactivated before the simulations at the initialization stage. These elements are activated layer-by-layer in case the two criteria are both satisfied:

1. If all of the quadrature point coordinates¹ along build direction, z , of the element are within the newly build layer (n^{th} layer) and formerly deposited layer ($n - 1^{th}$ layer);

$$(n - 1) d < z < n d \quad (16)$$

2. If the quiet elements satisfy the condition Ineq. (17) as in the reference [16];

$$\frac{\dot{Q}}{P \eta} \geq 0.05 \quad (17)$$

The volumetric heat source, \dot{Q} , is computed at every integration point based on heat source position and the coordinates of that integration point. The first activation criterion relates the layer height to the distance of the heat source from the baseplate to ensure the activation of the topmost elements. The second element activation criterion depends on the shape and position of the heat source as well as the position of the integration points of the element under concern. The energy density value of 0.05 permits activation of the elements in front of the melt pool, prior the moving heat source visits the elements. If all of the integration points of an element meet both these criteria only then it becomes activate.

4. Results and Discussion

Based on the results of the current study, the laser power clearly has a greater influence on the melt-pool dimensions in comparison to the scan speed that is consistent with literature findings. In this study, the powder mass flow rate was not compensated for either scan speed or laser power. Because of the lack of this compensation, variations in the layer thicknesses were measured. Previous literature has contradictory findings. For example Wolff et al. reported an increase in the laser power from 1000 W to 2000 W did not cause an increase in the height of the melt-pool [51]. On the other hand, a different study conducted at lower laser power range has shown increasing laser power values ranging from 400 W to 1000 W promoted increase in melt-pool heights for IN718 processed via DED method [52].

¹The top surface level of the baseplate along the build direction is set to zero ($z = 0$) in the FE model.

Micrographs of the cross-sections of single-tracks revealed some deviations from ideal such as the melt-pool offset from the center of the laser beam. This is believed to be due to the inaccuracies during fusion of the deposited layer on the baseplate. The inclination of the deposition head was measured but no offset inclination was measured on the nozzle.

Melt-pool morphology of a material was very sensitive to the process parameters similar to the reference [53]. The melt-pool expanded along with both width and depth directions with when the laser power was increased for almost all of the conditions. The exact opposite trend was observed when the scan speed increased. Previous literature defined the dilution, D [54] as the ratio of penetration depth, h , to the overall size of the melt zone that is the sum of the penetration depth, h , and the layer thickness, d as in Eq. (18). All of the melt-pool images in the current study show the presence of dilution. This finding was in agreement with the literature finding [51] that stated the dilution dominant DED process for laser power values over 1000 W.

$$D = h / (h + d) \quad (18)$$

The dilution was reported to show the bond quality between the deposited material and the substrate [54]. The amount of the dilution depends on the thermal history and melt-pool characteristics such as maximum temperature and cooling rate [55, 56]. Recent studies promoted the non-linear relation between the dilution and process parameters [46]. For dissimilar materials such as γ -TiAl alloy on titanium alloy substrate, low dilution values (around 0.06) were targeted to achieve greater micro-hardness values [57]. A minimum dilution rate of around 0.15 was required to achieve strong bonding between the layers for the multi-layer deposition on Ti6Al4V alloy [58]. In the case of deposition of nickel-based alloys, dilution values that were smaller than 0.6 were targeted because the higher values resulted in excessive melting of the substrate material which is undesired [59]. Wolff et al. obtained the dilution around 0.5 for laser deposition of IN718 on carbon steel substrate [51]. The dilution values in our study were calculated from the optical images, Table 3. The amount of dilution depended on both the laser power and the scan speed in case the the scan speed exceeded a certain threshold. For example, for scan speeds of 22.2 mm/s or higher, the dilution was insensitive to the laser power. The values of dilution obtained in the current study were in good agreement with the reported dilution values obtained for the same process parameters [51]. In this study, the in the clad height above the substrate as a function of increasing laser power was observed. This observation was consistent with literature findings [52] in which increasing laser power increased the clad height.

Figure 10 shows the comparison of in-situ thermal monitoring and finite element simulations of melt-pool morphology and temperature distributions for laser power and scan speed of 2500 W and 12.5 mm/s,

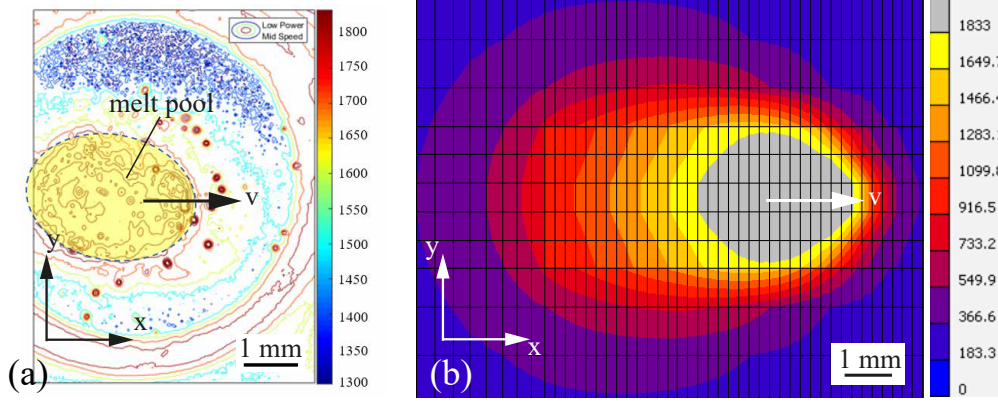


Figure 10: Melt-pool size (length and width) estimation for a single-track case; (a) experimental temperatures of in-situ IR camera measurements, (b) temperature distributions of the finite element simulation. Process parameters were 2500 W and 12.5 mm/s for laser power and scan speed, respectively.

respectively. The temperature in the core of the melt-pool was estimated to be approximately 1833 K. The in-situ temperature measurements well correlate with the simulation results. The melt-pool core temperature of 1833 K was used to identify the melt-zone boundaries. In Fig. 10(a), the measured size of the melt-zone slightly exceeded the boundary of the collected image, hence an elliptical shape was fitted to the melt-zones using image processing tools of MATLAB[®]. Using this methodology the width and the area of the melt-pool from the experiments and simulations were computed. The temperatures near the melt-pool gradually changed from almost 1650°C to below 400°C within a few millimeters at the proximity of the center of the heat source.

Table 3: Comparison of experimental measurements obtained from thermal camera images and thermal simulation results for single-track depositions.

scan speed [mm/s]	laser power [W]	dilution [-]	melt-pool area		error [%]
			exp. [mm ²]	sim. [mm ²]	
12.5	1500	0.39	6.88	6.48	-6
12.5	2000	0.37	9.46	8.80	-7
12.5	2500	0.33	12.7	11.2	-12
16.7	1500	0.47	6.28	5.36	-15
16.7	2000	0.48	8.19	7.1	-13
16.7	2500	0.52	10.5	10.12	-4
22.2	1500	0.46	5.04	4.2	-17
22.2	2000	0.46	5.24	4.94	-6
22.2	2500	0.46	8.74	8.79	1

Table 3 shows the area of melt-pool regions that were experimentally measured and simulated for different process parameters. Simulations slightly underestimated the amount of area of the melt-pool for all of the cases. This offset can be corrected by using a higher efficiency factor, η , in the simulations than conventional value of 0.6 [16]. The maximum difference in the melt-pool area was 17% for the low power and high speed case. This was the case with the lowest amount of melt-pool depth or dilution, Fig. 4. For the case with the

lowest dilution, the rest of the dimensions of the deposit increase revealing a larger melt-pool area.

Simulations of single tracks well predict the experimental melt-pool depth and width dimensions that were obtained by OM with a reasonable agreement. Fig. 11 demonstrates how the melt-pool dimensions were computed from both the experimental and simulation findings for only the laser power of 2500 W and scan speed of 12.5 mm/s. The melt-pool boundaries in the simulations were determined by the temperature contours of liquidus temperature of 1833 K while the experimental boundaries were measured from the baseplate ($z = 0$) level from the OM results.

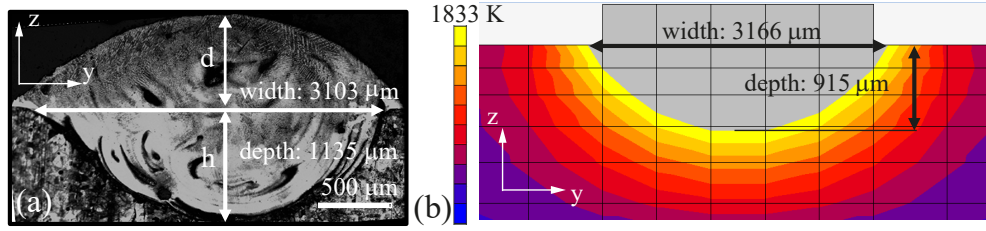


Figure 11: Melt-pool size (depth and width) comparison for single-track deposition: (a) experimental images of OM analysis, (b) temperature distributions of the finite element simulation. Process parameters were 2500 W and 12.5 mm/s for laser power and scan speed, respectively.

The dimensions of the melt-pool were measured using the method shown in Fig. 11. Table 4 shows the comparison of overall results of melt-pool dimensions for experimental measurements and simulation findings. Simulations overpredicted the melt-pool widths with a maximum error of 24%. Similarly, simulations underpredicted the melt-pool depths with a maximum error of 36%. One of the key factors causing this mismatch was the uniform layer thickness assumption that is used in the simulations. The layers were simulated by addition of a single element with a uniform thickness throughout the width of the build layer due to finite element modeling limitations. However, the thickness of the layer was not as uniform as in the experiments. Therefore, either the powder flow rates shall be adjusted to maintain uniform layer thickness in experiments, or the layer thickness in the experiments shall be consistent with the experimental values. In addition, the dilatation of the deposited layer due to thermal loads and corresponding displacements were not taken into consideration in the thermal model. The above-mentioned factors give rise to the difference in simulated and experimental melt-pool dimensions.

The numerical model well predicts the melt-pool dimensions for nearly all of the process parameters in comparison to the former studies. The clad height in DED process for IN718 was previously calculated with a 75% accuracy [51] which is almost the same with as demonstrated in the current study. Accordingly, Hernando et al. predicted the weld pool width and depth of IN718 with 90% and 96% accuracy rates, respectively [60]. The well-correlation of melt-pool dimensions for the numerical and experimental results show the predictive strength of the proposed method to estimate the overall interaction of the laser and the

Table 4: Melt-pool width and depth for single-track deposition. Comparison experimental OM measurements versus simulation results.

scan speed [mm/s]	laser power [W]	melt-pool width			melt-pool depth		
		exp. [μm]	sim. [μm]	error [%]	exp. [μm]	sim. [μm]	error [%]
12.5	1500	1755	2176	24	524	478	-9
12.5	2000	2397	2870	20	720	735	2
12.5	2500	3103	3166	2	1135	915	-19
16.7	1500	1632	1812	11	426	372	-13
16.7	2000	2154	2232	4	599	492	-18
16.7	2500	3055	2725	-11	738	665	-10
22.2	1500	1500	1506	1	305	264	-13
22.2	2000	1785	1675	-6	543	345	-36
22.2	2500	2264	2418	7	681	575	-16

baseplate material.

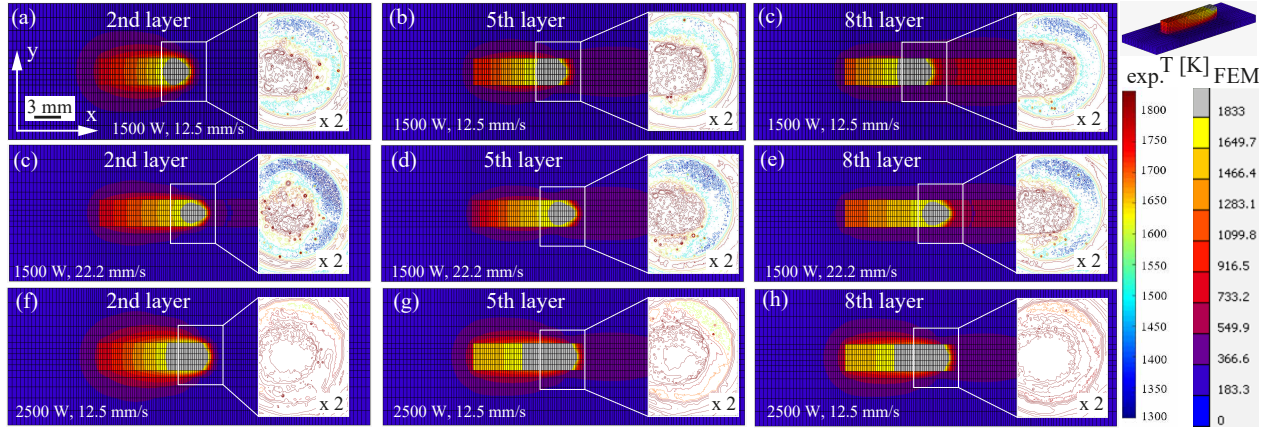


Figure 12: Temperature distributions of the simulations and in-situ melt-pool measurements for a multi-layer deposition. Top view of melt zone (a) 2nd layer, (b) 5th layer, (c) 8th layer for 1500 W laser power - 12.5 mm/s scan speed; (d) 2nd layer, (e) 5th layer, (f) 8th layer for 1500 W laser power - 22.2 mm/s scan speed; and (g) 2nd layer, (h) 5th layer, (i) 8th layer for 2500 W laser power - 12.5 mm/s scan speed.

Fig. 5 shows OM images of etched surface of the multi-layer deposition of IN718 alloy. The melt-pool dimensions were computed from these images for three different scan speeds of 12.5 mm/s, 16.7 mm/s and 22.2 mm/s and three different laser power values of 1500 W, 2000 W, and 2500 W. The total thicknesses of the deposited layer were 5.33 mm, 4.64 mm and 3.43 mm, respectively, that decreased with increasing scan speeds at the laser power of 1500 W. The total layer thickness gradually increased when the scanning speeds decrease from 22.2 mm/s to 16.7 mm/s and from 16.7 mm/s to 12.5 mm/s. Fig. 5 also show that the inter-layer fusion boundaries having a curved geometries between the consecutive layer that is partially due to the spreading of molten pool towards the layer underneath. The inter-layer fusion boundaries with the upper and lower limits were measured and tabulated in Table 5. The inter-layer fusion distance does not change with decreasing scan speeds and are $278.4 \pm 72.8 \mu\text{m}$, $340 \pm 32.7 \mu\text{m}$, and $391.2 \pm 86.7 \mu\text{m}$, respectively. However, less variation in the inter-layer fusion was obtained in the case of 16.7 mm/s scanning

speed. The inter-layer fusion boundaries were attributed to the difference in the dendrite structures or a combination of weak segregation banding and solute partitioning in the heat affected zone according to the previous studies [61, 62]. The uniform distance between inter-layer fusion boundaries indicate; i) the dendrite morphology remaining the same or ii) presence of segregation banding combined with solute partitioning in the heat affected zone.

Table 5: Comparison of melt-pool area; experimental measurements obtained from in-situ thermal imaging vs. thermal simulations for multiple layer deposition.

scan speed [mm/s]	laser power [W]	layer no.	melt-pool area		
			exp. [mm ²]	sim. [mm ²]	error [%]
12,5	1500	2	6,43	6,22	-3.3
12,5	1500	5	7,28	7,20	-1.1
12,5	1500	8	8,70	7,76	-10.8
22,5	1500	2	5,52	4,92	-10.9
22,5	1500	5	5,81	5,73	-1.3
22,5	1500	8	6,33	6,28	-0.8
12,5	2500	2	12,87	11,02	-14.4
12,5	2500	5	14,40	13,05	-9.4
12,5	2500	8	15,85	15,54	-2.0

The in-situ thermal measurements were used to compute the area of melt-pool and to compare the melt-pool sizes that were obtained from the process simulations for multi-layer deposits. Fig. 12 shows the melt-pool images on 2nd, 5th, and 8th layers of a multi-layer deposits of eight total layers during thermal simulations and corresponding in-situ temperature measurements. One of the important observations is that the area and the geometry of melt-pool geometry increases as the distance from the baseplate increases that is consistent in both simulation and experimental findings.

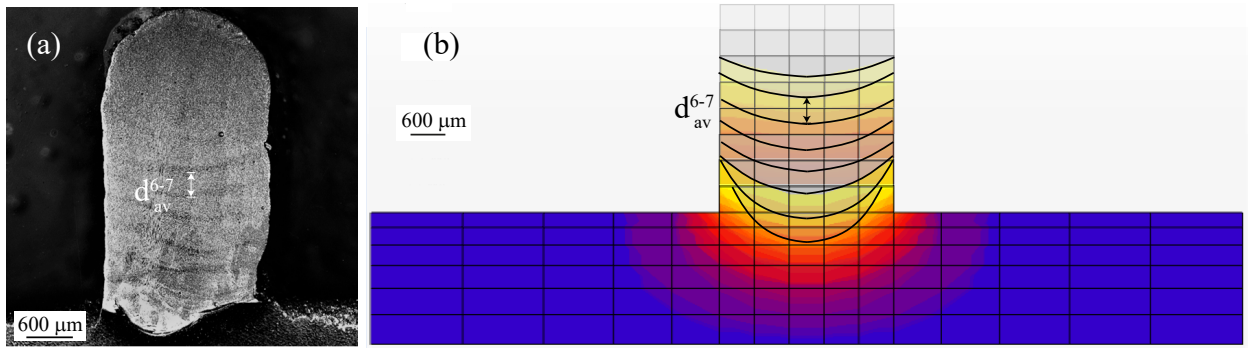


Figure 13: Average inter-layer fusion distance, example distance between the layers 6 and 7 is indicated with the symbol d_{av}^{6-7} ; (a) Experimental from OM analysis, (b) Melt zones obtained by superimposing the results of FE simulations for the case with 1500 W laser power and 12.5 mm/s scan speed.

Table 5 shows the comparison of the dimensions for the multi-layer deposits in Fig. 13. The deviation in the melt-pool area decreases at first, and then increases with the addition of layers. Simulations underestimated the area of the melt-pool slightly for all of the cases. The maximum deviation from the

experiments was approximately 15% thereby revealing a good correlation between the simulations and experiments. Ramping up the laser power increases the area of the melt-pool, while raising the scan speed decreases the area of the melt-pool. The melt zone patterns show good correlation with the proposed FE process model as demonstrated.

The analysis of the experimental OM results of multi-layer deposits were used to compute the inter-layer fusion distance between consecutive layers. Fig. 13 shows the superposition of the results for consecutive layers that was used to identify the inter-layer fusion distance from the analysis of cross-sections by OM and simulation results. The boundary between 6th and 7th layers was clearly visible, Fig. 13(a). However, not all of the inter-layer fusion boundaries were noticeable from the experimental micrographs. Apart from that, the melt-pool had an increased curvature between the baseplate and build material fusion boundary in comparison to the higher layers with decreasing cusps. This observation was noticeable in both the experiments and simulations. This time, inter-layer fusion boundaries were as not perfectly aligned and symmetric with respect to the center of the build layer in the experiments due to existing imperfections during deposition. However, a good agreement between the simulation results and the experimental measurements is discernible.

5. Conclusions

A thermal process simulation model for DED process that efficiently includes the surface heat losses as a volumetric heat sink term is developed and the findings for different process parameters compared to the experimental findings for melt-pool dimensions. Experiments include in-situ thermal measurements and ex-situ analysis of cross-sections of the samples that were produced under different process conditions. The important conclusions are listed as follows:

- Thermal process model uses a method in which the surface heat losses were expressed in terms of a volumetric heat sink term to eliminate the need for redefinition of free surfaces after the addition of each layer. This method incorporates convective, radiative, and evaporative surface heat losses efficiently by reducing the computation of surface fluxes.
- The maximum difference of the melt-pool area between the in-situ thermal measurements and simulation findings for single layer deposits reaches up to 17%.
- The predicted melt-pool depth and width has a maximum deviation of 36% and 24%, respectively.
- Melt-pool dimensions and inter-layer fusion boundaries of multi-layer deposition between the experiments and simulations has approximately a maximum of 15% different revealing the predictive capacity

of the thermal model.

- The thermal model predictions can be improved by considering the effect of varying layer thickness with varying process parameters. Either the experimentally powder mass flow rate shall be adjusted to compensate to obtain the desired layer thickness or the actual experimentally observed magnitude of the layer thickness shall be used in the simulations.

6. Acknowledgement

Authors kindly acknowledge efforts of M.Sc. Ragip Orkun Secer for the manufacturing of the samples. Graduate student (K.D.) acknowledges the Teaching Assistant scholarship provided by Faculty of Engineering and Natural Sciences of Sabanci University.

7. Appendix

7.1. Baseplate properties

The material properties of SS316L are shown in Table 6 [63].

Table 6: Thermo-physical properties of SS316L [63].

phase	T [K]	$\rho_{s,l}$ [kg/m ³]	$C_{p\ s,l}$ [J/K/kg]	$k_{s,l}$ [W/m/K]
solid	300	7954	499	13.96
solid	400	7910	512	15.53
solid	500	7864	525	17.10
solid	600	7818	538	18.68
solid	700	7771	552	20.25
solid	800	7723	565	21.82
solid	900	7674	579	23.39
solid	1000	7624	592	24.96
solid	1100	7574	605	26.53
solid	1200	7523	618	28.10
solid	1300	7471	632	29.67
solid	1400	7419	645	31.25
solid	1500	7365	658	32.82
solid	1600	7311	671	34.39
solid	1700	7256	685	35.96
liquid	1750	6979	770	17.98
liquid	1800	6920	770	18.31
liquid	1900	6857	770	18.64
liquid	2000	6791	770	18.97
liquid	2100	6721	770	19.30

7.2. Build material properties

The material consists of three different states; powder, liquid, and, solid. f_s is used an indicator to account for these different material states (fluid: $f_s = 0$, solid $f_s = 1$).

Any property in the fluid-solid state transformation regime, excluding the powder state, is computed by the rule of mixtures. Eq. (19) shows an example calculation for the density of the matter, ρ , using the density of solid, ρ_s , and liquid, ρ_l , phases.

$$\rho = f_s \rho_s + (1 - f_s) \rho_l \quad (19)$$

Table 7 shows the solid volume fraction during heating and cooling.

Table 7: Solid volume fraction, f_s , as a function of temperature [K] during melting of IN 718 [63].

f_s	0	0.1	0.2	0.3	0.4	0.5	0.6	0.7	0.8	0.9	0.95	1
heating	1346	1341	1336	1331	1326	1319	1311	1302	1290	1279	1266	1250
cooling	1335	1332	1328	1324.5	1320	1315	1310	1300	1291	1277	1263	-

Emissivity values are selected according to the reference [64] for IN 718 material, Table 8.

Table 8: Emissivity, ϵ_s , vs. temperature for IN718 [64].

T	[K]	543	558	757	873	882	1016	1067	1119	1281	1369
ϵ_s	[W/m ² /K]	0.23	0.24	0.26	0.28	0.28	0.30	0.31	0.31	0.32	0.33

The material properties of IN718 for solid and liquid phases are shown in Table 9. These values are the recommended material properties from the reference [63].

Table 9: Thermo-physical properties of IN718 [63].

phase	T [K]	$\rho_{s,l}$ [kg/m ³]	$C_{p\ s,l}$ [J/K/kg]	$k_{s,l}$ [W/m/K]
solid	298	8190	435	8.9
solid	373	8160	455	10.8
solid	473	8118	479	12.9
solid	573	8079	497	15.2
solid	673	8040	515	17.4
solid	773	8001	527	18.7
solid	873	7962	558	20.8
solid	973	7925	568	21.9
solid	1073	7884	680	26.9
solid	1173	7845	640	25.8
solid	1273	7806	620	26.7
solid	1373	7767	640	28.3
solid	1443	7727	650	29.3
liquid	1609	7400	720	29.6
liquid	1673	7340	720	29.6
liquid	1773	7250	720	29.6
liquid	1873	7160	720	29.6

References

- [1] J.-P. Kruth, M.-C. Leu, T. Nakagawa, Progress in additive manufacturing and rapid prototyping, CIRP Annals-Manufacturing Technology 47 (2) (1998) 525–540.

- [2] M. Isik, J. D. Avila, A. Bandyopadhyay, Alumina and tricalcium phosphate added coCr alloy for load-bearing implants, *Additive Manufacturing* 36 (2020) 101553.
- [3] J. D. Avila, M. Isik, A. Bandyopadhyay, Titanium–silicon on coCr alloy for load-bearing implants using directed energy deposition-based additive manufacturing, *ACS Applied Materials & Interfaces* 12 (46) (2020) 51263–51272.
- [4] T. DebRoy, H. Wei, J. Zuback, T. Mukherjee, J. Elmer, J. Milewski, A. M. Beese, A. Wilson-Heid, A. De, W. Zhang, Additive manufacturing of metallic components—process, structure and properties, *Progress in Materials Science* 92 (2018) 112–224.
- [5] H. X. Nguyen, H. Suen, B. Poudel, P. Kwon, H. Chung, Development of an innovative, high speed, large-scaled, and affordable metal additive manufacturing process, *CIRP Annals* 69 (1) (2020) 177–180.
- [6] M. Megahed, H.-W. Mindt, N. N'Dri, H. Duan, O. Desmaison, Metal additive-manufacturing process and residual stress modeling, *Integrating Materials and Manufacturing Innovation* 5 (1) (2016) 61–93.
- [7] M. Galati, L. Iuliano, A literature review of powder-based electron beam melting focusing on numerical simulations, *Additive Manufacturing* 19 (2018) 1–20.
- [8] A. Gisario, M. Kazarian, F. Martina, M. Mehrpouya, Metal additive manufacturing in the commercial aviation industry: A review, *Journal of Manufacturing Systems* 53 (2019) 124–149.
- [9] A. Bandyopadhyay, A. Shivaram, M. Isik, J. D. Avila, W. S. Dernell, S. Bose, Additively manufactured calcium phosphate reinforced coCrMo alloy: Bio-tribological and biocompatibility evaluation for load-bearing implants, *Additive Manufacturing* 28 (2019) 312–324.
- [10] J. M. Wilson, C. Piya, Y. C. Shin, F. Zhao, K. Ramani, Remanufacturing of turbine blades by laser direct deposition with its energy and environmental impact analysis, *Journal of Cleaner Production* 80 (2014) 170–178.
- [11] A. Saboori, A. Aversa, G. Marchese, S. Biamino, M. Lombardi, P. Fino, Application of directed energy deposition-based additive manufacturing in repair, *Applied Sciences* 9 (16) (2019) 3316.
- [12] T. Yamazaki, Development of a hybrid multi-tasking machine tool: integration of additive manufacturing technology with cnc machining, *Procedia Cirp* 42 (2016) 81–86.
- [13] N. Shamsaei, A. Yadollahi, L. Bian, S. M. Thompson, An overview of direct laser deposition for additive manufacturing; part ii: Mechanical behavior, process parameter optimization and control, *Additive Manufacturing* 8 (2015) 12–35.

- [14] A. Azarniya, X. G. Colera, M. J. Mirzaali, S. Sovizi, F. Bartolomeu, W. W. Wits, C. Y. Yap, J. Ahn, G. Miranda, F. S. Silva, et al., Additive manufacturing of ti-6al-4v parts through laser metal deposition (lmd): Process, microstructure, and mechanical properties, *Journal of Alloys and Compounds* 804 (2019) 163–191.
- [15] S. Wolff, S. Lin, E. J. Faierson, W. K. Liu, G. J. Wagner, J. Cao, A framework to link localized cooling and properties of directed energy deposition (ded)-processed ti-6al-4v, *Acta Materialia* 132 (2017) 106–117.
- [16] E. R. Denlinger, thermo-mechanical model development and experimental validation for metallic parts in additive manufacturing, Ph.D. thesis (2015).
- [17] S. Waqar, K. Guo, J. Sun, Fem analysis of thermal and residual stress profile in selective laser melting of 316l stainless steel, *Journal of Manufacturing Processes* 66 (2021) 81–100.
- [18] P. Promoppatum, S.-C. Yao, Influence of scanning length and energy input on residual stress reduction in metal additive manufacturing: Numerical and experimental studies, *Journal of Manufacturing Processes* 49 (2020) 247–259.
- [19] X. Liang, W. Dong, Q. Chen, A. C. To, On incorporating scanning strategy effects into the modified inherent strain modeling framework for laser powder bed fusion, *Additive Manufacturing* 37 (2021) 101648.
- [20] J. Robinson, I. Ashton, P. Fox, E. Jones, C. Sutcliffe, Determination of the effect of scan strategy on residual stress in laser powder bed fusion additive manufacturing, *Additive Manufacturing* 23 (2018) 13–24.
- [21] J. S. Weaver, J. C. Heigel, B. M. Lane, Laser spot size and scaling laws for laser beam additive manufacturing, *Journal of Manufacturing Processes* 73 (2022) 26–39.
- [22] M. S. Ghorashi, G. H. Farrahi, M. R. Movahhedy, Considering cyclic plasticity to predict residual stresses in laser cladding of inconel 718 multi bead samples, *Journal of Manufacturing Processes* 42 (2019) 149–158.
- [23] T. Mukherjee, W. Zhang, T. DebRoy, An improved prediction of residual stresses and distortion in additive manufacturing, *Computational Materials Science* 126 (2017) 360–372.
- [24] T. Walker, C. Bennett, T. Lee, A. Clare, A validated analytical-numerical modelling strategy to predict residual stresses in single-track laser deposited in718, *International Journal of Mechanical Sciences* 151 (2019) 609–621.

- [25] A. Lundbäck, L.-E. Lindgren, Modelling of metal deposition, *Finite Elements in Analysis and Design* 47 (10) (2011) 1169–1177.
- [26] J. Goldak, A. Chakravarti, M. Bibby, A new finite element model for welding heat sources, *Metallurgical transactions B* 15 (2) (1984) 299–305.
- [27] M. Chiumenti, M. Cervera, A. Salmi, C. A. De Saracibar, N. Dialami, K. Matsui, Finite element modeling of multi-pass welding and shaped metal deposition processes, *Computer methods in applied mechanics and engineering* 199 (37-40) (2010) 2343–2359.
- [28] I. A. Roberts, C. Wang, R. Esterlein, M. Stanford, D. Mynors, A three-dimensional finite element analysis of the temperature field during laser melting of metal powders in additive layer manufacturing, *International Journal of Machine Tools and Manufacture* 49 (12-13) (2009) 916–923.
- [29] J. Heigel, P. Michaleris, E. W. Reutzel, Thermo-mechanical model development and validation of directed energy deposition additive manufacturing of ti-6al-4v, *Additive manufacturing* 5 (2015) 9–19.
- [30] Q. Yang, P. Zhang, L. Cheng, Z. Min, M. Chyu, A. C. To, Finite element modeling and validation of thermomechanical behavior of ti-6al-4v in directed energy deposition additive manufacturing, *Additive Manufacturing* 12 (2016) 169–177.
- [31] P. Michaleris, Modeling metal deposition in heat transfer analyses of additive manufacturing processes, *Finite Elements in Analysis and Design* 86 (2014) 51–60.
- [32] S. Liu, K.-M. Hong, C. Katinas, Y. C. Shin, Multiphysics modeling of phase transformation and microhardness evolution in laser direct deposited ti6al4v, *Journal of Manufacturing Processes* 45 (2019) 579–587.
- [33] S. A. Khairallah, A. T. Anderson, A. Rubenchik, W. E. King, Laser powder-bed fusion additive manufacturing: Physics of complex melt flow and formation mechanisms of pores, spatter, and denudation zones, *Acta Materialia* 108 (2016) 36–45.
- [34] J. Lee, V. Prabhu, Simulation modeling for optimal control of additive manufacturing processes, *Additive Manufacturing* 12 (2016) 197–203.
- [35] E. Mirkoohi, D. Li, H. Garmestani, S. Y. Liang, Residual stress modeling considering microstructure evolution in metal additive manufacturing, *Journal of Manufacturing Processes* 68 (2021) 383–397.

- [36] S. S. Joshi, S. Sharma, S. Mazumder, M. V. Pantawane, N. B. Dahotre, Solidification and microstructure evolution in additively manufactured h13 steel via directed energy deposition: Integrated experimental and computational approach, *Journal of Manufacturing Processes* 68 (2021) 852–866.
- [37] S. M. Thompson, L. Bian, N. Shamsaei, A. Yadollahi, An overview of direct laser deposition for additive manufacturing; part i: Transport phenomena, modeling and diagnostics, *Additive Manufacturing* 8 (2015) 36–62.
- [38] P. Peyre, P. Aubry, R. Fabbro, R. Neveu, A. Longuet, Analytical and numerical modelling of the direct metal deposition laser process, *Journal of Physics D: Applied Physics* 41 (2) (2008) 025403.
- [39] A.-I. García-Moreno, J.-M. Alvarado-Orozco, J. Ibarra-Medina, E. Martínez-Franco, In-process monitoring of the melt-pool motion during continuous-wave laser metal deposition, *Journal of Manufacturing Processes* 65 (2021) 42–50.
- [40] S. K. Everton, M. Hirsch, P. Stravroulakis, R. K. Leach, A. T. Clare, Review of in-situ process monitoring and in-situ metrology for metal additive manufacturing, *Materials & Design* 95 (2016) 431–445.
- [41] K. Zhang, X. F. Shang, W. J. Liu, Realtime measurement of temperature field during direct laser deposition shaping, in: *Advanced Materials Research*, Vol. 143, Trans Tech Publ, 2011, pp. 521–526.
- [42] Z. Yan, W. Liu, Z. Tang, X. Liu, N. Zhang, Z. Wang, H. Zhang, Effect of thermal characteristics on distortion in laser cladding of aisi 316l, *Journal of Manufacturing Processes* 44 (2019) 309–318.
- [43] B. Carcel, J. Sampedro, I. Perez, E. Fernandez, J. A. Ramos, Improved laser metal deposition (lmd) of nickel base superalloys by pyrometry process control, in: *XVIII International Symposium On Gas Flow, Chemical Lasers, and High-power Lasers*, Vol. 7751, International Society for Optics and Photonics, 2010, p. 775123.
- [44] Z. Sun, W. Guo, L. Li, Numerical modelling of heat transfer, mass transport and microstructure formation in a high deposition rate laser directed energy deposition process, *Additive Manufacturing* 33 (2020) 101175.
- [45] R. Xie, G. Chen, Y. Zhao, S. Zhang, W. Yan, X. Lin, Q. Shi, In-situ observation and numerical simulation on the transient strain and distortion prediction during additive manufacturing, *Journal of Manufacturing Processes* 38 (2019) 494–501.
- [46] F. Alireza, T. Ehsan, K. Amir, D. Mohammad, Prediction of melt pool depth and dilution in laser powder deposition, *Journal of Physics D: Applied Physics* 39 (12) (2006) 2613–2623.

- [47] K. D. Traxel, D. Malihi, K. Starkey, A. Bandyopadhyay, Model-driven directed-energy-deposition process workflow incorporating powder flowrate as key parameter, *Manufacturing Letters* 25 (2020) 88–92.
- [48] Y. Lee, W. Zhang, Modeling of heat transfer, fluid flow and solidification microstructure of nickel-base superalloy fabricated by laser powder bed fusion, *Additive Manufacturing* 12 (2016) 178–188.
- [49] L. Parry, I. Ashcroft, R. D. Wildman, Understanding the effect of laser scan strategy on residual stress in selective laser melting through thermo-mechanical simulation, *Additive Manufacturing* 12 (2016) 1–15.
- [50] Users handbook: MSC.Marc, Volume D: User Subroutines and Special Routines, MSC Software Corporation, 2020.
- [51] S. J. Wolff, Z. Gan, S. Lin, J. L. Bennett, W. Yan, G. Hyatt, K. F. Ehmann, G. J. Wagner, W. K. Liu, J. Cao, Experimentally validated predictions of thermal history and microhardness in laser-deposited inconel 718 on carbon steel, *Additive Manufacturing* 27 (2019) 540–551.
- [52] T. Petrat, C. Brunner-Schwer, B. Graf, M. Rethmeier, Microstructure of inconel 718 parts with constant mass energy input manufactured with direct energy deposition, *Procedia Manufacturing* 36 (2019) 256–266, 17th Nordic Laser Materials Processing Conference - NOLAMP17.
- [53] L. Jichang, L. Lijun, Effects of process variables on laser direct formation of thin wall, *Optics & Laser Technology* 39 (2) (2007) 231–236.
- [54] S. F. C. Ehsan Toyserkani, Amir Khajepour, *Laser Cladding*, CRC Press, 2004.
- [55] J. L. Bennett, S. J. Wolff, G. Hyatt, K. Ehmann, J. Cao, Thermal effect on clad dimension for laser deposited inconel 718, *Journal of Manufacturing Processes* 28 (2017) 550–557, sI: NAMRC 45.
- [56] M. H. Farshidianfar, A. Khajepour, A. P. Gerlich, Effect of real-time cooling rate on microstructure in laser additive manufacturing, *Journal of Materials Processing Technology* 231 (2016) 468–478.
- [57] I. N. Maliutina, H. Si-Mohand, R. Piolet, F. Missemer, A. I. Popelyukh, N. S. Belousova, P. Bertrand, Laser cladding of γ -tial intermetallic alloy on titanium alloy substrates, *Metallurgical and Materials Transactions A* 47 (2016) 378–387.
- [58] T. Mukherjee, J. Zuback, A. De, T. DebRoy, Printability of alloys for additive manufacturing, *Scientific Reports* 6 (1) (2016) 19717.
- [59] C.-M. Lin, Relationships between microstructures and properties of buffer layer with inconel 52m clad on aisi 316l stainless steel by gtaw processing, *Surface and Coatings Technology* 228 (2013) 234–241.

- 608 [60] I. Hernando, J. I. Arrizubieta, A. Lamikiz, E. Ukar, Numerical model for predicting bead geometry and
609 microstructure in laser beam welding of inconel 718 sheets, *Metals* 8 (7) (2018).
- 610 [61] A. Ho, H. Zhao, J. W. Fellowes, F. Martina, A. E. Davis, P. B. Prangnell, On the origin of microstructural
611 banding in ti-6al4v wire-arc based high deposition rate additive manufacturing, *Acta Materialia* 166
612 (2019) 306–323.
- 613 [62] C. E. Seow, H. E. Coules, G. Wu, R. H. Khan, X. Xu, S. Williams, Wire+arc additively manufactured
614 inconel 718: Effect of post-deposition heat treatments on microstructure and tensile properties, *Materials*
615 & Design 183 (2019) 108157.
- 616 [63] K. C. Mills, Recommended values of thermophysical properties for selected commercial alloys, Woodhead
617 Publishing, 2002.
- 618 [64] G. Greene, C. Finfrock, T. Irvine Jr, Total hemispherical emissivity of oxidized inconel 718 in the
619 temperature range 300–1000 c, *Experimental Thermal and Fluid Science* 22 (3-4) (2000) 145–153.